| | |
|---|---|
| **Article Type:** | Invited Methods Collection - JoVE Produced Video |
| **Manuscript Number:** | JoVE62102R2 |
| **Full Title:** | Biplanar Videoradiography to Study the Wrist and Distal Radioulnar Joints |
| **Corresponding Author:** | Bardiya Akhbari, Ph.D. Candidate<br>Brown University<br>Providence, RI UNITED STATES |
| **Corresponding Author's Institution:** | Brown University |
| **Corresponding Author E-Mail:** | bardiya_akhbari@brown.edu |
| **Order of Authors:** | Bardiya Akhbari, Ph.D. Candidate |
| | Amy Morton |
| | Douglas Moore |
| | Joseph Crisco |
| **Additional Information:** | |

| Question | Response |
|---|---|
| Please specify the section of the submitted manuscript. | Bioengineering |
| Please indicate whether this article will be Standard Access or Open Access. | Standard Access (US$2,400) |
| Please indicate the **city, state/province, and country** where this article will be **filmed**. Please do not use abbreviations. | Providence, RI, USA |
| Please confirm that you have read and agree to the terms and conditions of the author license agreement that applies below: | I agree to the Author License Agreement |
| Please provide any comments to the journal here. | |

1 **TITLE:**
2 Biplanar Videoradiography to Study the Wrist and Distal Radioulnar Joints
3
4 **AUTHORS AND AFFILIATIONS:**
5 Bardiya Akhbari[1], Amy M Morton[2], Douglas C Moore[2], Joseph J Crisco[1,2]
6
7 [1] Center for Biomedical Engineering, Brown University, Providence, RI
8 [2] Department of Orthopedics, The Warren Alpert Medical School of Brown University and Rhode
9 Island Hospital, Providence, RI
10
11 **CORRESPONDING AUTHOR:**
12 Bardiya Akhbari
13 bardiya_akhbari@brown.edu
14
15 **EMAIL ADDRESSES OF CO-AUTHORS:**
16 Amy M. Morton          (amy_morton1@brown.edu)
17 Douglas C. Moore       (douglas_moore@brown.edu)
18 Joseph J. Crisco       (joseph_crisco@brown.edu)
19

20 **KEYWORDS:**
21 Biomechanics
22 Wrist
23 DRUJ
24 Videoradiography
25 Model-based
26 Tracking
27 Autoscoper
28 Total Wrist Arthroplasty
29 Kinematics
30

31 **SUMMARY**
32 Biplanar videoradiography (BVR) is an advanced imaging technique for understanding the three-
33 dimensional movement of skeletal bones and implants. Combining density-based image volumes
34 and videoradiographs of the distal upper extremity, BVR is used to study the in vivo motion of
35 the wrist and distal radioulnar joint, as well as joint arthroplasties.
36

37 **ABSTRACT**
38 Accurate measurement of skeletal kinematics in vivo is essential for understanding normal joint
39 function, the influence of pathology, disease progression, and the effects of treatments.
40 Measurement systems that use skin surface markers to infer skeletal motion have provided
41 important insight into normal and pathological kinematics, however, accurate arthrokinematics
42 cannot be attained using these systems, especially during dynamic activities. In the past two
43 decades, biplanar videoradiography (BVR) systems have enabled many researchers to directly
44 study the skeletal kinematics of the joints during activities of daily living. To implement BVR

45  systems for the distal upper extremity, videoradiographs of the distal radius and the hand are
46  acquired from two calibrated X-ray sources while a subject performs a designated task. Three-
47  dimensional (3D) rigid-body positions are computed from the videoradiographs via a best-fit
48  registration of 3D models to each BVR view. The 3D models are density-based image volumes of
49  the specific bone derived from independently acquired computed-tomography data. Utilizing
50  graphics processor units and high-performance computing systems, this model-based tracking
51  approach is shown to be fast and accurate in evaluating the wrist and distal radioulnar joint
52  biomechanics. In this study, we first summarized the previous studies that have established the
53  submillimeter and subdegree agreement of BVR with an in vitro optical motion capture system
54  in evaluating the wrist and distal radioulnar joint kinematics. Furthermore, we used BVR to
55  compute the center of rotation behavior of the wrist joint, to evaluate the articulation pattern of
56  the components of the implant upon one another, and to assess the dynamic change of ulnar
57  variance during pronosupination of the forearm. In the future, carpal bones may be captured in
58  greater detail with the addition of flat panel X-ray detectors, more sources (i.e., multiplanar
59  videoradiography), or innovative computer vision algorithms.
60
61  **INTRODUCTION**
62  Accurate measurement of skeletal kinematics in vivo is essential for understanding healthy and
63  replaced joint function, the influence of pathology, disease progression, and the effects of
64  treatments. Quantifying skeletal kinematics noninvasively at the joint surface (arthrokinematics)
65  is crucial to understand joint pathologies and diseases, such as osteoarthritis, but it is technically
66  challenging. Previously, techniques that use skin surface markers to infer skeletal motion have
67  provided important insight into healthy and pathological kinematics; however, accurate
68  arthrokinematics cannot be attained using these techniques, especially during dynamic activities
69  such as activities of daily living. These optical systems are inherently limited in accuracy because
70  of the skin movement relative to the underlying bones, the main source of error in human
71  movement analysis[1,2].
72
73  The current state-of-the-art methods for quantifying three-dimensional (3D) skeletal kinematics
74  are image-based tracking, namely, biplane videoradiography (BVR)[3], serial computed-
75  tomography (CT) volumes[4], and magnetic resonance imaging (MRI)[5]. Although regular 3D CT and
76  MRI-based technologies are highly accurate and accessible in many hospitals across the world,
77  they are incapable of measuring the dynamic motion of the joints. Imaging techniques such as
78  4D CT scanning[6] and dynamic MRI[7] have been developed in recent years to resolve this
79  shortcoming; however, these methods either expose patients to a high radiation dosage or suffer
80  from low temporal resolution.
81
82  Combining novel computer vision algorithms and traditional x-ray systems, BVR has been shown
83  to be accurate for multiple joints in animals and humans; resolved either with marker-based or
84  model-based tracking algorithms. Marker-based approaches track tantalum beads inserted into
85  bones or soft-tissue and are optimal for animal and in vitro testing. However, they are
86  prohibitively invasive for in vivo human research. Fortunately, improvements in model-based
87  tracking algorithms provide a viable alternative. Model-based BVR tracking approaches in
88  humans involve preparing the volumetric image sets acquired by CT or MRI in a static posture

89  and capturing the defined motions in the field-of-view of two X-rays. Most model-based tracking
90  applications then generate digitally reconstructed radiographs (DRR) of the bone or implant and
91  match them to feature-enhanced videoradiographs using metrics that demonstrate the similarity
92  between DRRs and videoradiographs[8]. This process is called "tracking" the bone or implant.
93
94  The primary output variables of tracking bones or implants are rigid body kinematics, from which
95  joint kinematics, ligament elongations[9,10], joint spacing as a surrogate for cartilage thickness[11],
96  joint contact[12,13], and other biomarkers can be computed. Recently, we documented the accuracy
97  of model-based tracking BVR in computing the biomechanics of the wrist, total wrist arthroplasty
98  (TWA), and distal radioulnar joint (DRUJ)[14,15]. In the following section, a detailed protocol of this
99  validated method for studying the motion of the skeletal wrist, total wrist arthroplasty, and the
100 distal radioulnar joint during various tasks is presented. We segment the density-based image
101 volumes of the bones and implants from the CT image volumes, track these partial image volumes
102 within the videoradiographs, and determine outcomes such as center of rotation, contact
103 pattern, and ulnar variance to demonstrate this method's strengths and limitations.
104
105 **PROTOCOL**
106
107 This study was approved by the Institutional Review Board (IRB) of Lifespan - Rhode Island
108 Hospital, an AAHRPP accredited IRB. A total of 16 patients provided signed informed consent
109 according to institutional guidelines.
110
111 **1.      Data acquisition**
112
113 1.1.     Computed tomography (CT)
114
115 1.1.1.   Prepare the subjects for the CT.
116
117 NOTE: For the accuracy evaluation[14,15], 6 intact forearms from four cadaver specimens (70.5 ±
118 12.3 yrs., 4 rights, 2 females) and 1 forearm (49 yrs., right, female) with a total wrist arthroplasty
119 were used. For the in vivo study[16], 10 volunteers with healthy wrists (57.0 ± 5.2 years, eight
120 females, nine right-hand dominant), and 6 patients (74.7 ± 5.6 years, two females, two right, four
121 dominant wrists) with a total wrist arthroplasty were enrolled.
122
123 1.1.2.  To image each subject[4], acquire a CT scan of the distal forearm with a 25 cm data
124 collection diameter and reconstruct with a 20 cm field-of-view using the Bone Plus convolution
125 algorithm by a 16-slice clinical CT scanner. Use tube settings of 80 kVp and 80 mA. Limit the
126 forearm exposure to approximately 7 cm proximal of the distal radius surface to the distal
127 phalanges.
128
129 NOTE: In this study, resulting voxel dimensions of the image were 0.39 × 0.39 mm$^2$ in the
130 transverse plane of the forearm, and 0.625 mm along the forearm's long axis.
131

132  1.1.3.  Transfer the acquired CT images to the laboratory's computer using a HIPPA-approved
133  protocol in Digital Imaging and Communications in Medicine (DICOM) format.

134
135  **1.2.  Biplanar videoradiography (BVR)**

136
137  1.2.1.  Experimental setup (**Figure 1**). To enable a field-of-view diameter able to capture the
138  distal radius, distal ulna, carpal bones, and metacarpals as well as a perspective to minimize bony
139  occlusions in various wrist postures, position the image intensifiers (IIs) below the forearms, and
140  set the angle between them at 110° (X-ray sources aimed downward to the corresponding IIs at
141  55° orientation relative to the ground).

142
143  1.2.1.1.  Generate the X-rays in continuous mode with an exposure setting ranging from 65
144  to 75 kV depending on visibility of the bones/implant and 80 mA. Adjust the source-to-image
145  distances of both X-Ray-II pairs at approximately 130 cm, and the source-to-hand distances at 90
146  cm.

147
148  NOTE: In this study, subjects wore an x-ray protective lead apron, a thyroid collar shield neck
149  cover, and a digital dosimeter in the laboratory. All researchers were standing behind a lead
150  shielding glass during the experiment.

151
152  1.2.1.2.  Place a trestle between IIs, and use it for placement of items (e.g., doorknob,
153  hammer, pitcher) for the volunteers.

154
155  [Place Figure 1 Here]

156
157  1.2.2.  Undistortion grid (**Figure 2A**). Because the external electromagnetic fields affect the
158  internal behavior of the X-ray beams (i.e., electron paths), the radiographic images suffer from
159  nonlinear pincushion and S-shaped distortions[17]. To remove these distortions, use an image of a
160  flat piece of precision perforated sheet metal (i.e., undistortion grid)[18,19]. Place undistortion grids
161  onto the IIs and capture their images both before and after videoradiography data. Save these
162  images as 8-bit TIFF images for both X-ray sources.

163
164  1.2.3.  Calibration (**Figure 2B**). Calibration of the X-ray sources is necessary to compute the 3D
165  coordinates of the objects (bones or implants)[20]. Use images of a 3D object with a known
166  geometry, which has regularly spaced radio-opaque spheres, to generate a relationship between
167  the X-ray source's position and orientation in 3D space and the image space (i.e., radiographs). A
168  cubical object (i.e., calibration cube) made from acrylic sheets and spacers with steel spheres are
169  effective and accurate for BVR settings[19].

170
171  1.2.3.1.  Capture radiographs of the calibration cube[18] in various orientations 4 times
172  before performing the experiment and 4 times after the experiment. The post-experiment
173  calibrations serve to confirm that the experimental setup remains unchanged throughout the
174  experiment. Save all images as 8-bit TIFF images for both X-ray sources.

175

176 [Place **Figure 2** Here]
177
178 1.2.4. Tasks description. Define various tasks to capture the wrist motion during flexion-
179 extension, radial-ulnar deviation, and circumduction[16]. Describe DRUJ motion tasks as forearm
180 rotation from a holding pose to full pronation or to full supination defined as rotation of a T-
181 handle doorknob in clockwise and counter clockwise directions[21]. Acquire videoradiographs of
182 the wrist at its neutral pose (i.e., neutral static task). Capture the neutral pose when the back of
183 the hand was coplanar with the back of the forearm.
184
185 NOTE: In the starting posture of all tasks, the shoulder was in adduction, the elbow was supported
186 at the joint level, and the forearm was unconstrained and in its neutral rotation. Tasks of flexion-
187 extension and radial-ulnar deviation were described as the rotation of the palm relative to the
188 volar-dorsal and radial-ulnar sides of the hand, respectively. Circumduction was described as the
189 wrist motion that aimed to achieve maximum active range-of-motion in every direction.
190
191 1.2.5. Videoradiograph acquisition. Acquire videoradiographs at a rate of 200 Hz with the
192 camera shutter speed set at 500 µs. Record two seconds of imaging for each task. Store
193 videoradiographs acquired from each X-ray source as CINE video in an 8-bit format.
194
195 NOTE: In this study, the radiographs were 1760×1760 pixels in image size and had a resolution of
196 approximately 0.22×0.22mm per pixel.
197
198 NOTE: Current X-ray sources have an option to magnify the field-of-view (FOV); however, in this
199 study, the magnified mode offered by the hardware was not used. Based on the task description,
200 this capability might enable you to acquire higher resolution outputs. If this feature is used, the
201 Undistortion Grid and Calibration steps must be captured in this mode.
202
203 1.3.     **Optical motion capture (OMC) – accuracy study**
204
205 1.3.1. Use the optical motion capture (OMC) data acquisition protocol described in previous
206 studies[14,15]. Directly attach two marker clusters, each with four 9.5 mm diameter retro-reflective
207 marker spheres, to the third metacarpal and radius bones. Capture markers movement by 8
208 optical motion capture cameras. Synchronize the start of the OMC data acquisition with the BVR
209 by an active low external trigger.
210
211 **2.      Data Processing**
212
213 2.1.     Computed tomography (CT)
214
215 2.1.1. DICOM anonymization. Anonymize the DICOMs and import them into image processing
216 software for 3D modeling (e.g., Mimics Materialise). In the software, from the **File** toolbar, open
217 the **Anonymize** window. When the new window is opened, select **Anonymize All Images** from
218 the left tab, and press the **Anonymize** button on the bottom right.
219

220    2.1.2. Segmentation (**Figure 3**). Segment the bones or implants of interest following a previously
221    described methodology[16,22,23].

223    2.1.2.1.        Briefly, from the **Segment** toolbar, select the **Threshold** option, and choose the
224    predefined threshold sets of **Bone** when the window is opened. After the thresholded mask is
225    created, use the **Split Mask** option, and manually paint the **Regions** of bones or implant's
226    components.

228    2.1.2.2.        When all regions are painted, click **OK** and wait for the software to generate the
229    masks for each bone and implant's components automatically. Check all masks to ensure they
230    are covering the intended regions completely. If not, use **Edit Masks** option to modify the regions
231    manually and one-by-one.

233    NOTE: To study the wrist joint, the 2$^{nd}$, and 3$^{rd}$ metacarpals and radius bones, and to study the
234    DRUJ, the radius and ulna should be segmented and separated from the rest of bones. For the
235    implants, the radial component and the carpal component with its screws should be segmented.
236    Optionally, the capitate and other bones can be segmented for post-processing stages.

238    [Place Figure 3 Here]

240    2.1.3. Segmentation - radial component only. Due to streak artifacts of the surface of the radial
241    component in the CT images, the radial component model cannot be segmented from the
242    images. Thus, use a 3D surface scanner to generate the 3D model of the explanted radial
243    component. Transfer this model to the image registration software and register to the
244    segmentation of the radial component using Mimics Materialise default's method.

246    NOTE: In this study, we used a surface scanner with the resolution of 0.1 mm. The implant was
247    placed on a table, and the 3D scanner was manually moved around the implant to capture all
248    external surfaces.

250    2.1.4. Partial image volumes. The tracking software requires a segmented body of interest to be
251    input as a density-based image volume. To create this partial volume, generate a full-mask of the
252    image volume containing all grey values by selecting the **Threshold** option from the **Segment**
253    toolbar. Adjust the threshold values from the minimum to the maximum grey-values.

255    2.1.4.1.        Then, use the **Boolean Operators** option, and **Subtract** the segmented volume of
256    the bone or implant of interest from the generated full-mask. Change the color of this partial
257    volume's mask to black (RGB: 0.0/0.0/0.0) because the registration software accepts only
258    grayscale image volumes. Export the mask as a DICOM by selecting **Export DICOM…** in the
259    software. The output is an image volume of the isolated bone or implant.

261    2.1.5. Three-Dimensional Models. Convert the segmented masks to triangulated meshed 3D
262    surface models by selecting the **Calculate 3D** option, with the **Optimal Resolution**. Export these
263    models in VRML format, containing the 3D location of vertices (points) and their order of

connections. The models are generated for coordinate system construction and further visualization.

## 2.2.  **Videoradiography Pre-processing**

2.2.1.  XMALab[18] Import. For each subject, create a new trial in XMALab software. Assign the folder paths to Undistortion Grid images and 8 sets of calibration images in the **New Trial** dialog.

NOTE: If the X-ray sources are flipped throughout the capture, the flip option must be checked in the XMALab software.

2.2.2.  De-distortion. To de-distort radiographs, after the trial was created and the software had opened the grid images in the Undistortion workspace, click the **Compute Undistortion** button. XMALab automatically determines and displays the de-distorted images of the grids. Once the centers of all holes were detected by the software, change the workspace in the top left menu to the **Calibration** workspace. For more information and for assistance in debugging potential issues, see the reference[24].

2.2.3.  Calibration. In this stage, XMALab software determines the calibration matrices. In XMALab, model the X-rays sources as a pinhole camera with intrinsic and extrinsic parameters, such as focal length, source's center, and source-to-image distances, and calibration stage is a process that determines these metrics[18]. To calibrate, select each of the 4 reference items placed in the calibration cube for all sets of images and for each view. In the setup, these references were Pyramid, Jack, Dome, and Helix (**Figure 2B**). If the software did not automatically find the points, press **Compute Calibration**. After all calibration images were calibrated, select **Optimize Camera Setup**.

2.2.4.  Exporting Calibration Matrices. After optimization, sort through all 8 calibration sets (i.e., the 4 sets that were captured prior to the experiment and the 4 sets that were captured after the experiment) and select the image set with smallest error undistorted. Find this value by pressing the information option on the top-right corner of each calibration window. On the image with the lowest error, export the images by selecting the **MayaCams 2.0** option from the **File-Export** menu. For more information and to debug possible problems see the reference[20].

2.2.5.  Videoradiography Undistortion. Change the workspace to **Marker tracking** and load the videoradiographs that were captured in CINE-format by pressing the **+** icon. After the loading process is completed, export the undistorted trial images by selecting **Undistorted Trial Images** from the **File-Export** menu.

## 2.3.  **Model-based Tracking (Figure 4)**

2.3.1.  Enhancing Features of Radiographs/DRRs (**Figure 4A-B**). Enhancing the image features using filters is a necessary step to achieve an accurate match. Define four filters of contrast (intensity detection), Sobel (edge detection), Gaussian (blurring/smoother), and Sharpen

308     (boldening the edges) in the software. These filters can be selected by right-clicking on the **Rad**
309     **Renderer** or **DRR Renderer** objects shown in the top-left widget.

310

311     NOTE: In this study, the edges of the bones' images on the radiographs were enhanced using a
312     Sobel filter with a scale factor of 3 and a blend value of 0.4. Additionally, a contrast filter with an
313     alpha (for image contrast) of 2.5, and beta (for image brightness) of 0.9 was used to further
314     improve the quality of the radiographs. To match the DRRs with the radiograph, a ray intensity
315     value of 0.35 was utilized with a Sobel filter with 0.1 blend value and 1.7 scale factor.

316

317     2.3.2.    Manual Initialization. Move the DRR of each bone and component using its **Pivot point** to
318     achieve the best match possible between DRR and radiographs. **Pivot point** helps users to rotate
319     and translate the selected DRR in the bottom-left widget. This step is necessary because the
320     position of the bone or implant must be initialized at least once, and at least for the first frame,
321     before performing the optimization. Press **W** to move the DRR in translation mode and press **E**
322     to rotate the DRR.

323

324     NOTE: Changing the pivot point location is not typically necessary, but it is possible using the
325     **Move Pivot** option of the toolbar.

326

327     2.3.3.    Optimization. Press **C** or click on **Track Current** button from the toolbar to find the most
328     similar match between the DRR and the radiographs. The software's default procedure uses the
329     normalized cross-correlation (NCC) cost function and both particle swarm optimization method
330     and downhill simplex procedures[26, 27]. This process is also called matching or tracking step. The
331     optimization procedure can also be executed via **Tracking Dialog**. To do so, press **Tracking Dialog**
332     option from the toolbar. When the new window is opened, change the From frame and to frame
333     to 0, and press **OK**.

334

335     NOTE: NCC is a function that measures the similarity between the radiographs and DRRs, and an
336     NCC value closer to 0 demonstrated a better match. However, achieving this value completely
337     depended on the image filters and capture qualities. The value of NCC can be observed in the
338     "Terminal Window".

339

340     2.3.4.   Matching Process – First Pass. After the first frame is automatically optimized, open the
341     **Tracking Dialog**, change the **From frame** to 0, and change the **to frame** to the last frame number
342     (this can be located on the right-bottom). The default matching process of the software uses the
343     **Current frame** as the initial position of DRR for matching process. The optimization process uses
344     particle swarm optimization (PSO) method within a region of 3 mm and 3° of the initial position.

345

346     2.3.5.   Matching Process – Final Pass (**Figure 4C**). Because the automated matching process may
347     fail due to a poor initialization or low-quality choice of filters, check all frames manually to ensure
348     the optimization has been executed correctly. If the DRR and radiographs are not matched
349     correctly, repeat the steps described in section 2.3.2 and 2.3.3.

350

351 NOTE: Tracking the wrist was first performed with the model combining the second and third
352 metacarpals (MC2-MC3) to reduce the effects of bone overlap and improve the matching
353 accuracy. After locating the combined DRR position and rotation in the radiographs, the matched
354 and optimized MC2-MC3 locations were transformed to the MC3 partial image volume, and initial
355 positions of the MC3 were seeded. Using these seeded positions, the MC3 was tracked. Similar
356 to MC3, the radius, ulna, radial component, and carpal component in the videoradiographs
357 during all tasks were also tracked.
358
359 [Place Figure 4 Here]
360
361 2.3.6.   Data Reduction. Based on the frame rate and the radiographic images quality, filtering
362 approaches such as moving average method (with a span of 5 frames) could be utilized. To do so,
363 from the toolbar menu, select **Tracking-Advanced Dialog**, and click on **Smooth** button. This
364 approach was used for all captures in this study.
365
366 2.3.7.   Exporting Bone/Implant Positions. After each bone is matched to the radiographs and all
367 frames are optimized, export 4x4 transformation matrices of the DRRs in the X-ray world by
368 clicking on the **Save Tracking** button and selecting the matrix format output. This transformation
369 matrix defines the rotation and translation of the partial image volume of the bone/implant in
370 the calibrated X-ray world coordinate system and can be used for additional processing and
371 motion calculation. The coordinate system of the partial image volume must be transferred to
372 the anatomical coordinate system for meaningful biomechanical analysis.
373
374 **3.      Data Analysis**
375
376 3.1.      **Coordinate Systems (Figure 5).** To report kinematics, construct coordinate systems (CS)
377 for bones and implant components based on their anatomical and geometrical landmarks. After
378 these CS were constructed, register the models that are in the new CS to the surface models that
379 were generated in **Section 2.1.4** using iterative closest point algorithm. This one-to-one
380 registration computes a new 4x4 transformation matrix that will be used for kinematics
381 calculation.
382
383 NOTE: In this study, the CS for the radius, ulna, third metacarpal, carpal component, radial
384 component, polyethylene cap, and capitate were created using methods that have been
385 described previously[16, 22, 23].
386
387 [Place Figure 5 Here]
388
389 3.2.      **Kinematics.** In this study, define wrist motion as motion of the MC3 relative to the radius,
390 and the kinematic data was reported relative to the neutral wrist position.
391
392 3.2.1.   For the DRUJ analysis, calculate helical axis of motion (HAM) parameters[28] to describe the
393 kinematics as the relative motion of the radius CS in the ulna CS, with respect to the neutral
394 pose.

395
396  3.2.2.  Use HAM analysis to determine the center of rotation (COR) of the wrist in flexion-
397  extension and radial-ulnar deviation.
398
399  3.2.3.  To describe the one-dimensional proximal-distal shift of the COR, define the projected
400  COR for the healthy wrists as a point on the central axis of the capitate bone which had the
401  shortest distance from the screw axis of rotation[16].
402
403  3.2.4.  Decompose the HAM rotation in the ulnar coordinate system using the HAM screw axis,
404  and calculate the pronation (positive) and supination (negative) of the forearm. The neutral pose
405  was defined when pronation-supination (PS) was zero.
406
407  3.2.5.  Lastly, define ulnar variance (UV) as the distance between the ulnar fovea and the sigmoid
408  notch on the radius.
409
410  3.3.    **Articulation Pattern**
411
412  3.3.1.  In this study, calculate ontact patterns between the polyethylene cap and radial
413  component using the wrist kinematics and component-specific distance fields[29].
414
415  3.3.2.  Calculate distance fields for each 3D surface model as a volumetric array of signed
416  distances from the surface.
417
418  3.3.3.  Calculate the distance fields' proximity values on the surface of the polyethylene cap and
419  radial component for each posture.
420
421  3.3.4.  To obtain the contact patch between the components, adjust these proximity values to
422  the resolution of the acquisition system. Use a distance exclusion threshold of 0.70 mm to
423  determine the resolution.
424
425  3.4.    **Statistical Analysis**
426
427  3.4.1.  Use Bland-Altman to evaluate the accuracy by demonstrating the bias (mean differences)
428  and 95% limit of agreement (bias ± 1.96SD) between BVR and OMC[14, 30].
429
430  3.4.2.  Use a generalized linear model (GLM) to describe the center of rotation behavior of the
431  healthy wrist, and to find a relationship between the change in UV and PS ($UV = p_1 \times PS^2 + p_2 \times PS$),
432  where $p_1$ and $p_2$ were coefficients that were optimized using linear regression. Use root-mean-
433  squared-error (RMSE) metric to evaluate the model's accuracy.
434
435  **REPRESENTATIVE RESULTS**
436  Selection of model-based tracking 2D-to-3D image registration software depends in part on
437  access to graphics processor unit (GPU) and high-performance computing (HPC) systems. These
438  programs have different pipelines, and as of now, there is no common methodology among the

439    programs. In this study, an open-source 2D-to-3D image registration program, Autoscoper,
440    developed at Brown University was used[25]. The choice of open-source makes it possible for the
441    investigators to modify and automate their pipeline. In this software, radiographic images are
442    named "Rad Renderer" and digitally reconstructed radiographs are named "DRR Renderer". The
443    features of these images were enhanced with four type of filters, and the software was capable
444    of performing the matching process using 2 optimization algorithms (particle swarm and downhill
445    simplex). Two similarity measures (cost functions) of normalized cross correlation (NCC) and sum
446    of absolute difference (SAD) were also pre-defined in this software.

448    The bias between BVR and OMC was submillimeter and sub-degree for the wrist, the replaced
449    wrist (TWA), and DRUJ[14, 15]. The 95% limits of agreement between the methods were -1.5 to 1.5°
450    in rotation and -1.2 to 1.4 mm in translation for the wrist (**Table 1**), -1.0 to 0.8° in rotation and -
451    0.8 to 0.9 mm in translation for the TWA (**Table 2**), and -1.1 to 0.9° in rotation and -1.0 to 1.4 mm
452    in translation for the DRUJ motion (**Table 3**). The ulnar variance was also measured throughout
453    pronation and supination with 95% limits of agreement of -0.5 to 0.7 mm and -0.4 mm to 0.7
454    mm, respectively.

456    For the wrist, the dynamic projected center of rotation was assessed throughout all wrist motion
457    on the capitate (**Figure 6A**)[8]. The COR of the wrist was located on the proximal side of the capitate
458    with an average of 21.5 mm and 20.8 mm in flexion and extension, respectively. The COR was
459    located at mid-capitate with an average of 13.9 mm for both radial and ulnar deviation range-of-
460    motion.

462    For the total wrist arthroplasty, the contact articulation pattern of the components with a
463    resolution of 0.4 mm was described (**Figure 6B**). In this experiment, the center of contact moved
464    in an area of 34.2 ± 13.1 mm about the dorsal-radial side of the polyethylene cap's CS, and it
465    moved in an area of 21.9 ± 8.0 mm on the radial component.

467    For the DRUJ, it was observed that the ulnar variance dynamically changes and it increases
468    (becomes more positive) in pronation (**Figure 6C**). The ulnar variance dynamic change was
469    modeled as a 2nd-degree polynomial with an average $p_1$ of 0.00033, and $p_2$ of 0.0276. The fitted
470    equation had an RMSE of 0.60 mm, and the subject-specific polynomial models achieved a high
471    consistency with RMSEs that were less than 0.59 mm.

473    [Place Figure 6 Here]

475    **FIGURE AND TABLE LEGENDS**
476    **Figure 1.** Experimental Setup.

478    **Figure 2. A**) Undistortion Grid. **B**) Calibration Cube and its Reference Items.

480    **Figure 3.** Computed-tomography Image of the Wrist and Reconstructed Models of Radius, Third
481    metacarpal, and Ulna.
482

**Figure 4. A**) Captured Radiograph of an X-ray Source with Digitally Reconstructed Radiographs (DRRs) of the Bones. **B**) Enhanced (Filtered) Radiograph and DRRs. **C**) Matched DRRs after Optimization Process.

**Figure 5.** Coordinate Systems of the Bones and Implant's Components.

**Figure 6. A**) Wrist Center of Rotation (COR) on Capitate. **B**) Contact Pattern of a Total Wrist Arthroplasty during Circumduction. **C**) Change in Ulnar Variance.

**Figure 7.** Occlusion Problem in Tracking Carpal Bones and Third Metacarpal.

**Table 1.** The bias and 95% limits-of-agreement between biplanar videoradiography and optical motion capture (gold-standard) in calculating wrist motion.

**Table 2.** The bias and 95% limits-of-agreement between biplanar videoradiography and optical motion capture (gold-standard) in calculating replaced wrist (TWA) motion.

**Table 3.** The bias and 95% limits-of-agreement between biplanar videoradiography and optical motion capture (gold-standard) in calculating distal radioulnar joint (DRUJ) motion.

**DISCUSSION**

Biplanar videoradiography (BVR) is an image-based method that can be used to measure bone and implant motion in the wrist and distal radioulnar joint with submillimeter and subdegree accuracy. In this study, BVR was used to identify an accurate pattern of projected COR for a healthy wrist as well as TWA contact patterns. Such findings can aid future designs of the total wrist replacements and can provide in vivo data for validation of computational of models. Using BVR, the nonlinear relationship of change in ulnar variance with forearm pronosupination was also observed, which could be helpful in treatment planning for DRUJ pathologies. Due to its dynamic capture and its high accuracy, BVR can be used to study wrist and DRUJ pathologies in various motions to recommend strategies for treatments and diagnosis.

To ensure accurate results, there are critical steps that need careful attention from the experimenters in both pre-processing and processing stages. Throughout the experiment, investigators need to be meticulous in calibrating the X-ray sources because the final output is dependent on the calibration matrices. Calibrating the X-ray sources multiple times, both before and after the experiment, will help investigators to ensure the calibration is accurate. Throughout processing, the optimization methods and cost functions, as well as the filters that are used on the radiographs and DRRs, can affect the outcome. Thus, it is best to keep these parameters fixed throughout a single project. Furthermore, model-based tracking is a time-consuming task on personal computers as these systems typically do not have powerful GPUs and cannot fully utilize the parallelization of CPUs, which can be offered by HPC systems. In this study, we suggested using Autoscoper, because it is an open-source software that can utilize the GPU and can be executed on HPC systems. Currently, this system is widely used by researchers across the world[31]. There are plans to upgrade the software package to SlicerAutoscoper in the near future, a

527   powerful software that can be used for analyzing both CT image data and BVR image data. With
528   this potential upgrade, investigators can streamline different methods of imaging acquisition.
529
530   Model-based tracking BVR is a powerful and accurate methodology. However, many steps in the
531   protocol during the experiment or at the post-processing stages might need additional
532   troubleshooting. The calibration stage can be arduous and labor-intensive if the reference points
533   are missing in the radiographic view. Furthermore, there are many methods for describing the
534   calibration parameters, and currently, there is no standard among the scientists who work on the
535   2D-to-3D image registration programs. In this protocol, OpenCV standards were used, which are
536   commonly implemented in the computer vision field, with the hope of creating consensus among
537   investigators across fields[32]. In Autoscoper, this standard is a text file containing the image size
538   in pixels, a 3x3 camera matrix, a 3x3 rotation matrix, and a 3x1 translation vector. (Rotation and
539   translation describe the X-ray source orientation and position in the world space). Additionally,
540   refining the results while tracking may seem trivial, but diligent observation of the NCC value and
541   how the cost function changes frame-by-frame is important in assuring optimal results. Finally,
542   the initialization stage is time-consuming and requires the user to have a good understanding of
543   the 3D spatial view of objects. To overcome this, we are currently developing a method to
544   automate or semi-automate the initialization stage for the bones of the hands.
545
546   There are three main limitations in using BVR to study the upper extremity. First, currently it is
547   difficult, or sometimes impossible, to track the small overlapping carpal bones in the radiographs
548   (**Figure 7**). It is also difficult to track the 3rd metacarpal bone during tasks in which all metacarpals
549   overlap, such as in full flexion or full extension. Therefore, carpal kinematics cannot be measured,
550   and an extra step for tracking the 3rd metacarpal is required. Second, the BVR method is time-
551   consuming, expensive, and requires constant supervision. Third, the radiation exposure to the
552   patients increases if they have to perform many tasks for a long time. Additional safety strategies
553   to limit exposure can be followed by checking exposures for each setup and using lead vests.
554   Typically, in our experimental set-up, our subjects were exposed to radiation at approximately
555   0.095 mSV per second.
556
557   [Place Figure 7 Here]
558
559   Image-based object tracking is the state-of-the-art for accurate quantification of 3D skeletal
560   motion, and biplanar videoradiography is an important method that enables researchers to study
561   the wrist, total wrist arthroplasty, and distal radioulnar joint in vivo. Although carpal bones
562   cannot be tracked optimally in BVR, methods such as multiplanar videoradiography can limit the
563   occlusion of the carpal bones. Alternative methods such as MRI and CT scanning can be used if
564   there is no need for high temporal resolution, and there is no need to study the motion for a long
565   time. Other methods such as optical motion capture can also be used when researchers can
566   eliminate motion artifact, which can only happen in in vitro biomechanical studies.
567
568   In this study, we demonstrated BVR usage for the wrist, total wrist arthroplasty, and distal
569   radioulnar joint. BVR has also been used to study the spine[33, 34], shoulder[35–39], elbow[40], hip[41],
570   knee[42–44], and foot and ankle[45–48]. In the upper extremity field, potential applications of BVR in

the research setting include following the progression of a disease and dynamically capturing bone and joint movement. This method can also be used to study the accuracy of implant movement with the hope of designing better implants or finding potential reasons for implant failure.

**DISCLOSURES**
We have no conflict of interest to declare.

**REFERENCES**
1. Leardini, A., Chiari, L., Croce, U.D., Cappozzo, A. Human movement analysis using stereophotogrammetry: Part 3. Soft tissue artifact assessment and compensation. *Gait & Posture*. **21** (2), 212–225 (2005).
2. Miranda, D.L., Rainbow, M.J., Crisco, J.J., Fleming, B.C. Kinematic differences between optical motion capture and biplanar videoradiography during a jump-cut maneuver. *Journal of biomechanics*. **46** (3), 567–573 (2013).
3. Tashman, S., Anderst, W. In vivo measurement of dynamic joint motion using high speed biplane radiography and CT: application to canine ACL deficiency. *Journal of Biomechanical Engineering*. **125** (2), 238–245 (2003).
4. Moore, D. C. et al. Computed Tomography Image-Based Kinematic Analysis: An Overview. *Handbook of Imaging in Biological Mechanics*. 115–126 (2014).
5. Fedorov, A. et al. 3D Slicer as an Image Computing Platform for the Quantitative Imaging Network. *Magnetic resonance imaging*. **30** (9), 1323–1341 (2012).
6. Choi, Y.S. et al. Four-dimensional real-time cine images of wrist joint kinematics using dual source CT with minimal time increment scanning. *Yonsei medical journal*. **54** (4), 1026–1032 (2013).
7. Boutin, R.D. et al. Real-Time Magnetic Resonance Imaging (MRI) during Active Wrist Motion—Initial Observations. *PLoS ONE*. **8** (12), e84004 (2013).
8. Miranda, D.L. et al. Static and Dynamic Error of a Biplanar Videoradiography System Using Marker-Based and Markerless Tracking Techniques. *Journal of Biomechanical Engineering*. **133** (12), 121002-121002–8 (2011).
9. Englander, Z.A. et al. In Vivo Anterior Cruciate Ligament Deformation During a Single-Legged Jump Measured by Magnetic Resonance Imaging and High-Speed Biplanar Radiography , In Vivo Anterior Cruciate Ligament Deformation During a Single-Legged Jump Measured by Magnetic Resonance Imaging and High-Speed Biplanar Radiography. *The American Journal of Sports Medicine*. **47** (13), 3166–3172 (2019).

614    10.    Englander, Z.A., Garrett, W.E., Spritzer, C.E., DeFrate, L.E. In vivo attachment site to
615    attachment site length and strain of the ACL and its bundles during the full gait cycle measured
616    by MRI and high-speed biplanar radiography. *Journal of Biomechanics*. **98**, 109443 (2020).
617    11.    Anderst, W.J., Les, C., Tashman, S. In vivo serial joint space measurements during
618    dynamic loading in a canine model of osteoarthritis. *Osteoarthritis and cartilage: Osteoarthritis*
619    *Research Society*. **13** (9), 808–816 (2005).
620    12.    Bey, M.J., Kline, S.K., Zauel, R., Kolowich, P.A., Lock, T.R. In Vivo Measurement of
621    Glenohumeral Joint Contact Patterns. *EURASIP journal on advances in signal processing*. **2010**
622    (2010).
623    13.    Anderst, W.J., Tashman, S. A method to estimate in vivo dynamic articular surface
624    interaction. *Journal of Biomechanics*. **36** (9), 1291–1299 (2003).
625    14.    Akhbari, B. et al. Accuracy of biplane videoradiography for quantifying dynamic wrist
626    kinematics. *Journal of Biomechanics*. **92**, 120–125 (2019).
627    15.    Akhbari, B. et al. Kinematic Accuracy in Tracking Total Wrist Arthroplasty with Biplane
628    Videoradiography using a CT-generated Model. *Journal of Biomechanical Engineering*. (2019).
629    16.    Akhbari, B. et al. Proximal-distal shift of the center of rotation in a total wrist
630    arthroplasty is more than twice of the healthy wrist. *Journal of Orthopaedic Research: Official*
631    *Publication of the Orthopaedic Research Society*. **38** (7), 1575–1586 (2020).
632    17.    Wang, J., Blackburn, T.J. The AAPM/RSNA Physics Tutorial for Residents. *RadioGraphics*.
633    **20** (5), 1471–1477 (2000).
634    18.    Knörlein, B.J., Baier, D.B., Gatesy, S.M., Laurence-Chasen, J.D., Brainerd, E.L. Validation
635    of XMALab software for marker-based XROMM. *The Journal of Experimental Biology*. **219** (23),
636    3701–3711 (2016).
637    19.    Brainerd, E.L. et al. X-ray reconstruction of moving morphology (XROMM): precision,
638    accuracy and applications in comparative biomechanics research. *Journal of experimental*
639    *zoology. Part A, Ecological genetics and physiology*. **313** (5), 262–279 (2010).
640    20.    Knörlein, B.J. X-ray Camera Calibration. *XROMM / XMALab / wiki*. at
641    <https://bitbucket.org/xromm/xmalab/wiki/X-ray%20Camera%20Calibration> (2020).
642    21.    Akhbari, B. et al. Biomechanics of the Distal Radioulnar Joint in In vivo Forearm
643    Pronosupination. *Journal of Wrist Surgery (Under Review)* (2020).
644    22.    Akhbari, B. et al. Predicting carpal bone kinematics using an expanded digital database
645    of wrist carpal bone anatomy and kinematics. *Journal of Orthopaedic Research: Official*
646    *Publication of the Orthopaedic Research Society*. (2019).
647    23.    Moore, D.C. et al. Three-dimensional in vivo kinematics of the distal radioulnar joint in
648    malunited distal radius fractures. *The Journal of Hand Surgery*. **27** (2), 233–242 (2002).
649    24.    Knörlein, B.J. Correct for Fluoroscope Distortion (X-ray images). *XROMM / XMALab /*
650    *wiki*. at
651    <https://bitbucket.org/xromm/xmalab/wiki/Correct%20for%20Fluoroscope%20Distortion%20(
652    X-ray%20images)> (2020).
653    25.    Akhbari, B., Knörlein, B., Loomis, A., Howison, M. *Autoscoper*. at
654    <https://simtk.org/projects/autoscoper>. Brown University. Providence, RI. (2019).
655    26.    Kennedy, J., Eberhart, R. *Particle swarm optimization*. (1995).
656    27.    Nelder, J.A., Mead, R. A Simplex Method for Function Minimization. *The Computer*
657    *Journal*. **7**, 308 (1965).

658    28.    Panjabi, M.; W.I. A Mathematical Approach for three-dimensional analysis of the
659    mechanics of the spine. *J Biomechanics*. **4**, 203–211 (1971).
660    29.    Marai, G.E. et al. Estimating joint contact areas and ligament lengths from bone
661    kinematics and surfaces. *IEEE transactions on bio-medical engineering*. **51** (5), 790–799 (2004).
662    30.    Bland, J.M., Altman, D.G. Measuring agreement in method comparison studies.
663    *Statistical methods in medical research*. **8** (2), 135–160 (1999).
664    31.    SimTk Autoscoper Downloads Summary. *Autoscoper (Bone/Implant Tracking Software)*.
665    at
666    <https://simtk.org/plugins/reports/index.php?type=group&reports=reports&group_id=1799>
667    (2020).
668    32.    Camera calibration With OpenCV. at
669    <https://docs.opencv.org/2.4/doc/tutorials/calib3d/camera_calibration/camera_calibration.ht
670    ml> (2020).
671    33.    Anderst, W.J., Lee, J.Y., Kang, J.D. In Vivo Cervical Facet Joint Capsule Deformation
672    During Flexion-Extension. *Spine*. **39** (8), E514–E520 (2014).
673    34.    Anderst, W.J., Vaidya, R., Tashman, S. A technique to measure three-dimensional in vivo
674    rotation of fused and adjacent lumbar vertebrae. *The Spine Journal*. **8** (6), 991–997 (2008).
675    35.    Mozingo, J.D. et al. Validation of imaging-based quantification of glenohumeral joint
676    kinematics using an unmodified clinical biplane fluoroscopy system. *Journal of Biomechanics*.
677    **71**, 306–312 (2018).
678    36.    Akbari-Shandiz, M. et al. MRI vs CT-based 2D-3D auto-registration accuracy for
679    quantifying shoulder motion using biplane video-radiography. *Journal of Biomechanics*. **82**,
680    375–380 (2019).
681    37.    Bey, M.J. et al. In vivo shoulder function after surgical repair of a torn rotator cuff:
682    glenohumeral joint mechanics, shoulder strength, clinical outcomes, and their interaction. *The*
683    *American journal of sports medicine*. **39** (10), 2117–2129 (2011).
684    38.    Bey, M.J., Kline, S.K., Zauel, R., Kolowich, P.A., Lock, T.R. In Vivo Measurement of
685    Glenohumeral Joint Contact Patterns. *EURASIP journal on advances in signal processing*. **2010**
686    (2010).
687    39.    Bey, M.J., Zauel, R., Brock, S.K., Tashman, S. Validation of a New Model-Based Tracking
688    Technique for Measuring Three-Dimensional, In Vivo Glenohumeral Joint Kinematics. *Journal of*
689    *biomechanical engineering*. **128** (4), 604–609 (2006).
690    40.    Fu, E. et al. Elbow Position Affects Distal Radioulnar Joint Kinematics. *The Journal of*
691    *Hand Surgery*. **34** (7), 1261–1268 (2009).
692    41.    Martin, D.E. et al. Model-Based Tracking of the Hip: Implications for Novel Analyses of
693    Hip Pathology. *The Journal of Arthroplasty*. **26** (1), 88–97 (2011).
694    42.    Miranda, D.L. et al. Static and Dynamic Error of a Biplanar Videoradiography System
695    Using Marker-Based and Markerless Tracking Techniques. *Journal of Biomechanical*
696    *Engineering*. **133** (12), 121002-121002–8 (2011).
697    43.    Stentz-Olesen, K. et al. Validation of static and dynamic radiostereometric analysis of
698    the knee joint using bone models from CT data. *Bone & Joint Research*. **6** (6), 376–384 (2017).
699    44.    Anderst, W., Zauel, R., Bishop, J., Demps, E., Tashman, S. Validation of Three-
700    Dimensional Model-Based Tibio-Femoral Tracking During Running. *Medical engineering &*
701    *physics*. **31** (1), 10–16 (2009).

702    45.    Kessler, S.E. et al. A Direct Comparison of Biplanar Videoradiography and Optical Motion
703    Capture for Foot and Ankle Kinematics. *Frontiers in Bioengineering and Biotechnology*. **7**, 199
704    (2019).
705    46.    Maharaj, J.N. et al. The Reliability of Foot and Ankle Bone and Joint Kinematics
706    Measured With Biplanar Videoradiography and Manual Scientific Rotoscoping. *Frontiers in
707    Bioengineering and Biotechnology*. **8**, 106 (2020).
708    47.    Ito, K. et al. Direct assessment of 3D foot bone kinematics using biplanar X-ray
709    fluoroscopy and an automatic model registration method. *Journal of Foot and Ankle Research*.
710    **8**, 21 (2015).
711    48.    Wang, B. et al. Accuracy and feasibility of high-speed dual fluoroscopy and model-based
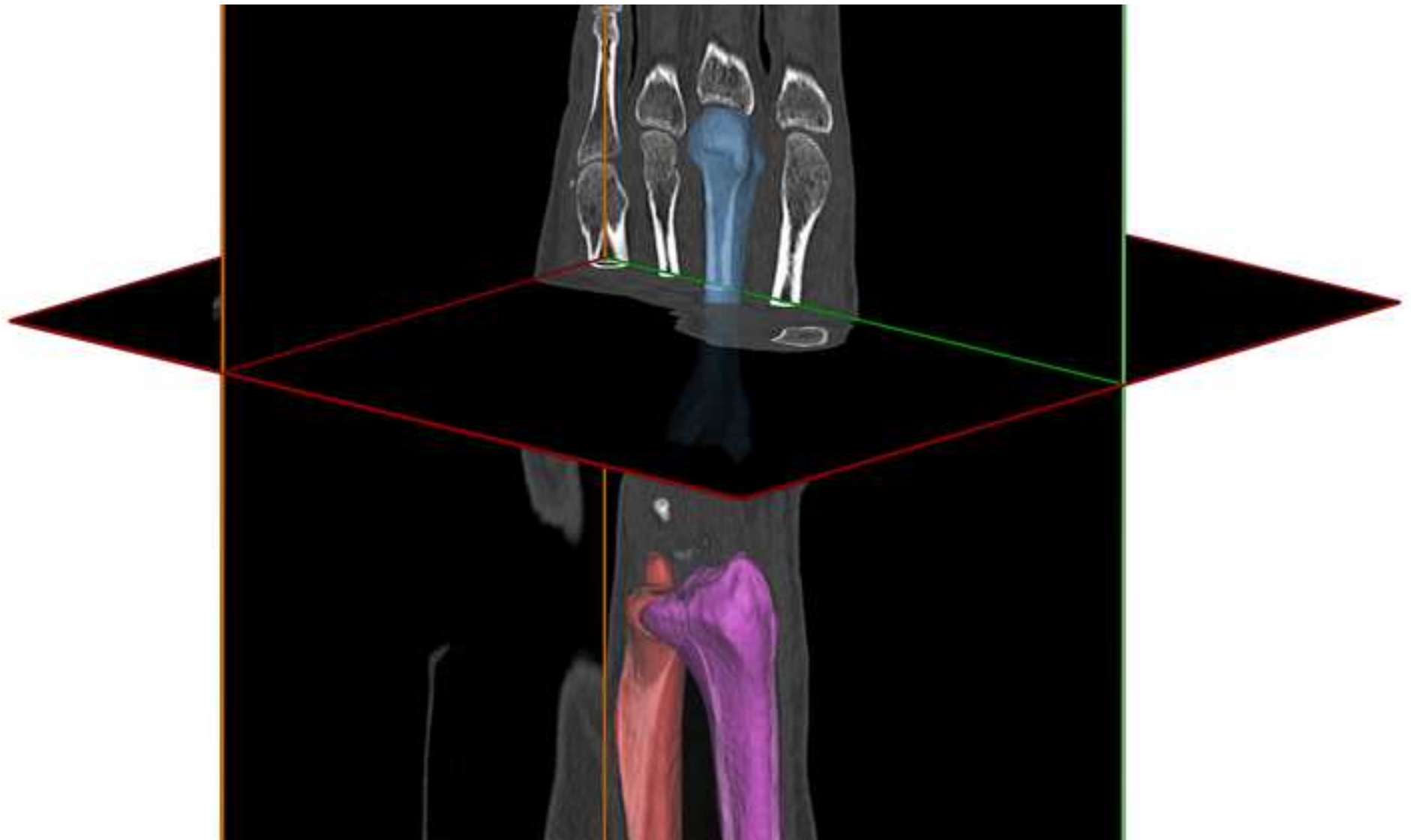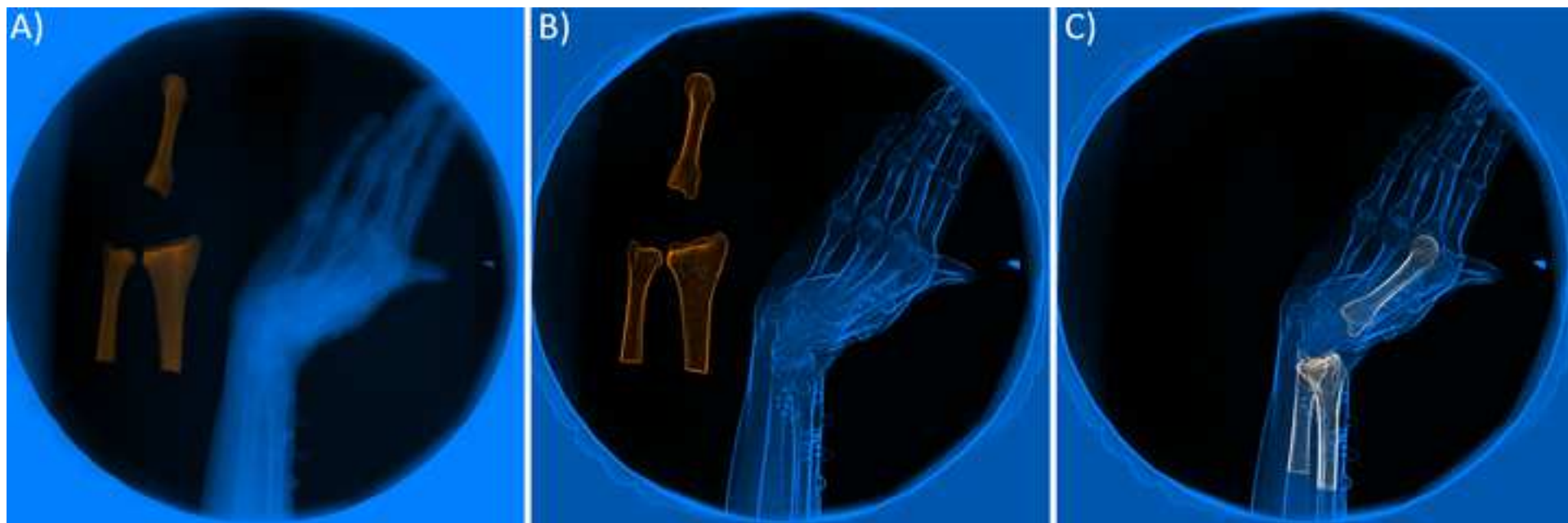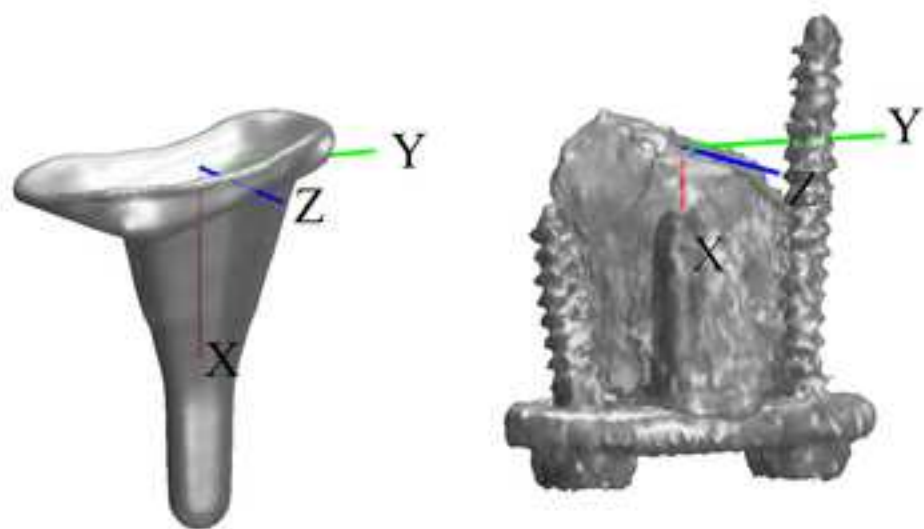712    tracking to measure in vivo ankle arthrokinematics. *Gait & Posture*. **41** (4), 888–893 (2015).
713

Inter-beam Angle = ~110°

XROMM Facility
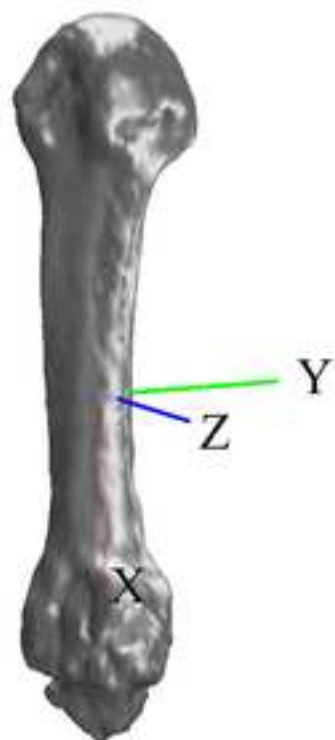xromm.org
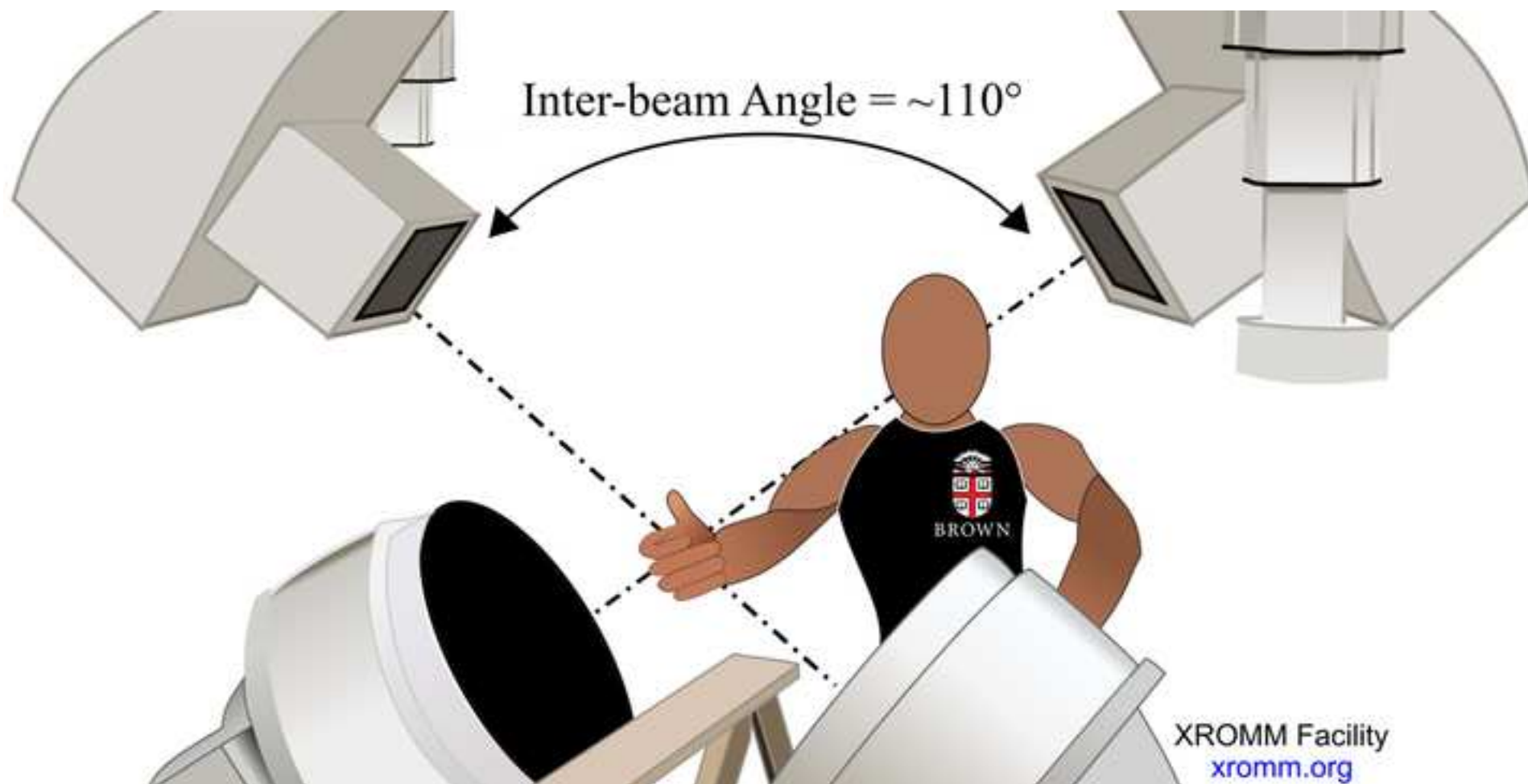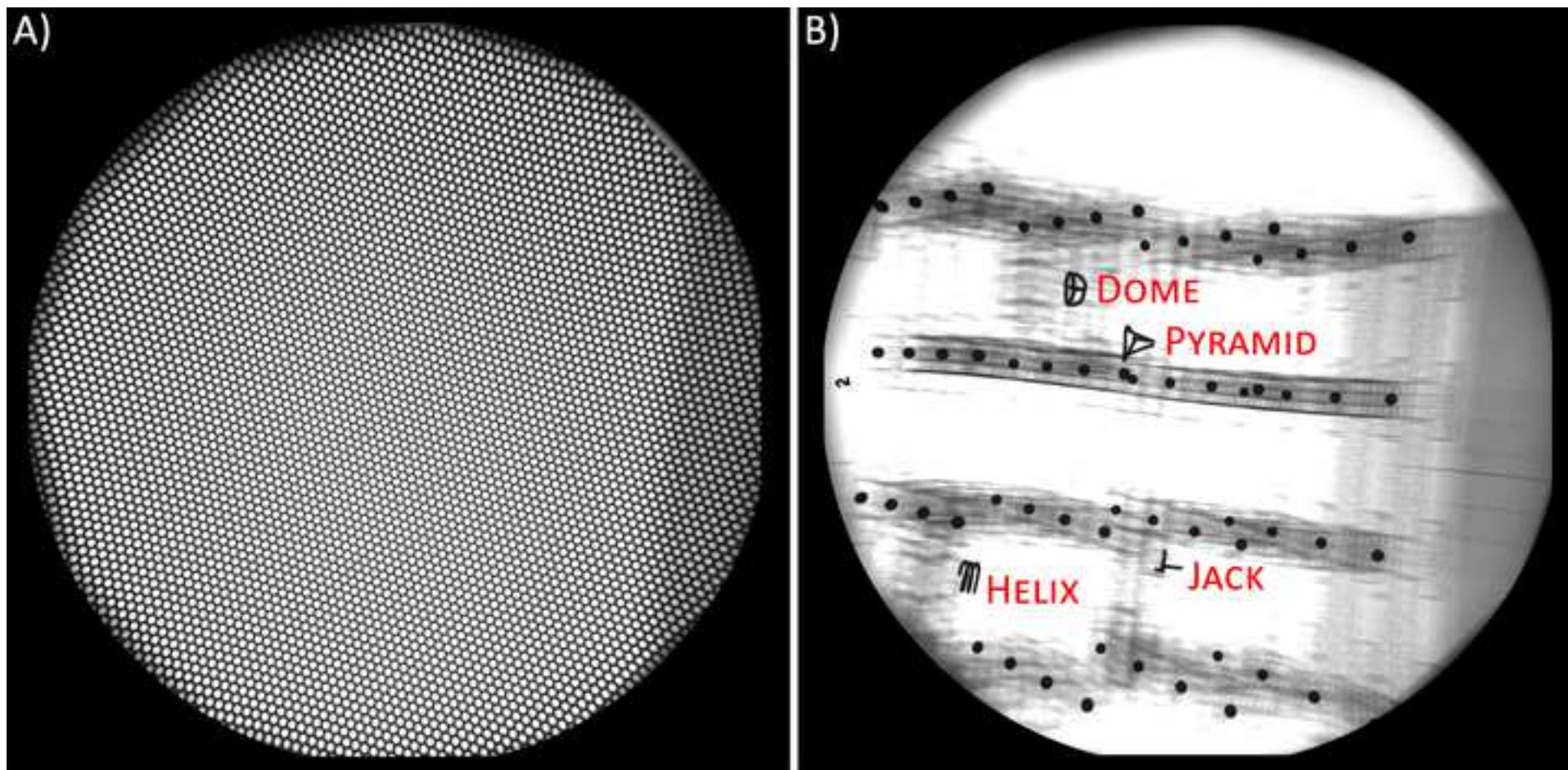
Figure 2

Figure 3

Figure 5
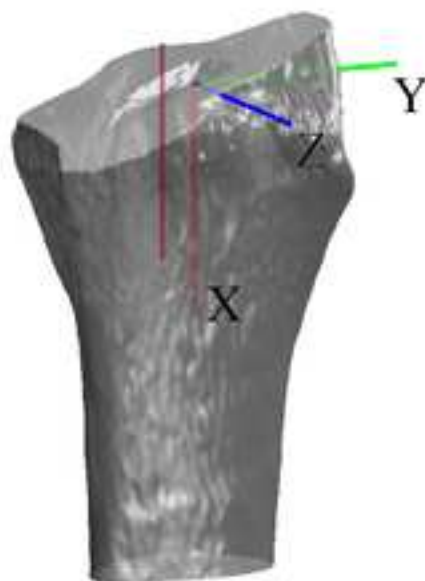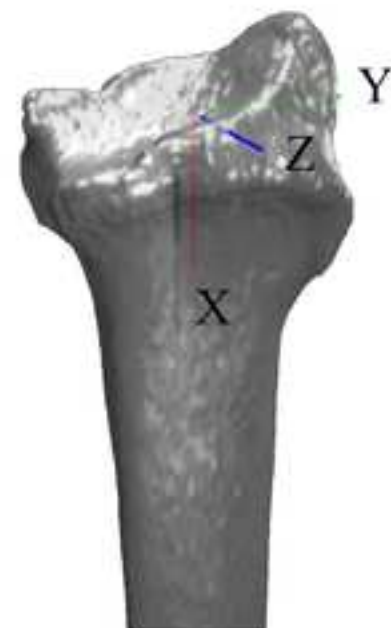
Radial Component

Carpal Component
(with resected Capitate)
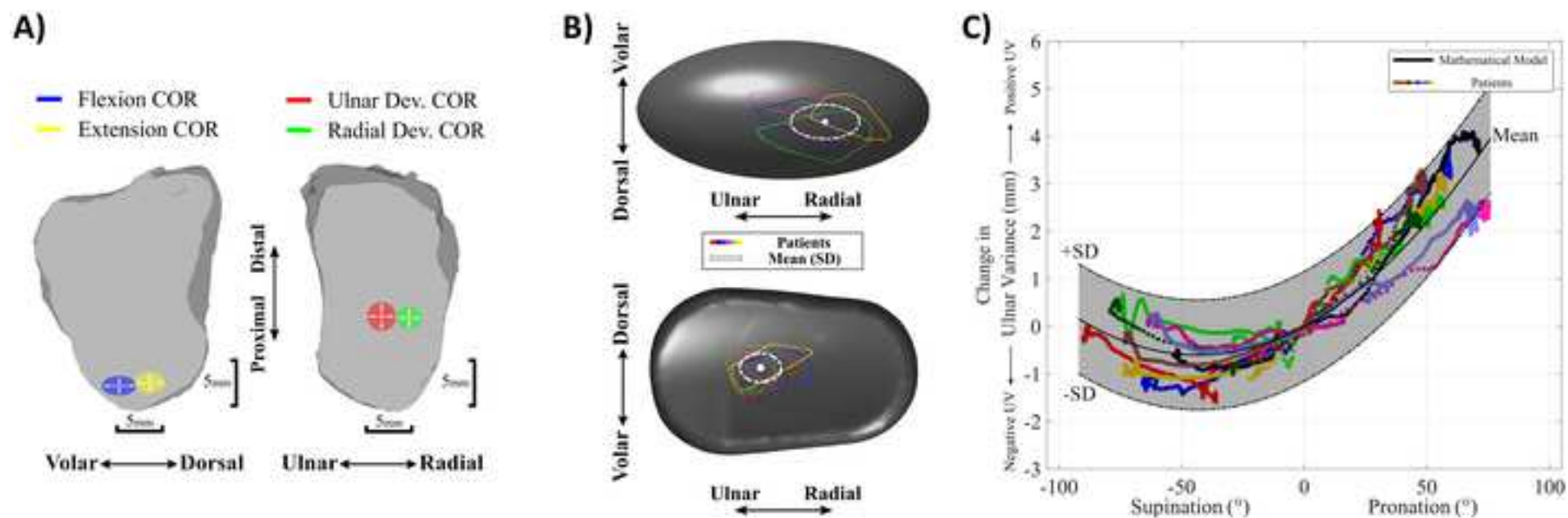
Third Metacarpal

Resected Radius

Radius

Figure 7

Table 1. Wrist

| Task | Overall Wrist Rotation (°) | | Overall Wrist Translation (mm) | |
|---|---|---|---|---|
| | Bias | LOA | Bias | LOA |
| Flexion-Extension | 0.1 | -1.3 — 1.5 | 0.1 | -1.2 — 1.4 |
| Radial-Ulnar Deviation | 0 | -1.5 — 1.5 | 0.2 | -0.6 — 1.0 |
| Circumduction | 0.1 | -1.2 — 1.4 | 0.1 | -1.1 — 1.3 |

Table 2. TWA

| Task | Overall TWA Rotation (°) | | Overall TWA Translation (mm) | |
|---|---|---|---|---|
| | Bias | LOA | Bias | LOA |
| Flexion-Extension | -0.1 | -1.0 — 0.8 | 0 | -0.6 — 0.9 |
| Radial-Ulnar Deviation | -0.1 | -0.7 — 0.5 | -0.2 | -0.8 — 0.4 |
| Circumduction | -0.2 | -1.0 — 0.6 | 0 | -0.5 — 0.6 |

| | Overall TWA Rotation (°) | | Overall TWA Translation (mm) | |
|---|---|---|---|---|
| | Bias | LOA | Bias | LOA |

Table 3. DRUJ

| Task | Overall DRUJ Rotation (°) | | Overall DRUJ Translation (mm) | |
|---|---|---|---|---|
| | Bias | LOA | Bias | LOA |
| Pronation | -0.1 | -1.1 — 0.9 | 0.4 | -0.5 — 1.4 |
| Supination | 0 | -0.8 — 0.8 | 0.2 | -1.0 — 1.3 |

| | Overall DRUJ Rotation (°) | | Overall DRUJ Translation (mm) | |
|---|---|---|---|---|
| | Bias | LOA | Bias | LOA |
| | -0.1 | -1.1 — 0.9 | -0.5 — 1.3 | |

| Name of Material/Equipment | Company | Catalog Number |
|---|---|---|
| 3D Surface Scanner | Artec 3D | Artec Space Spider™ |
| Autoscoper | Brown University | https://simtk.org/projects/autoscoper |
| CT Scanner | General Electric (GE) | Lightspeed 16 |
| Geomagic Wrap 3D | 3DSystems | Version 2017 |
| Graphics Processing Unit (GPU) | Nvidia | GeForce GTX 1080 |
| High-speed Video Cameras | Phantom | Version 10 |
| Image Intensifier | Dunlee | 40 cm diameter |
| ImageJ | Open-source (Brown University) | https://imagej.net/Fiji |
| Matlab | The MathWorks, Inc. | R2017a to R2020a |
| Mimics | Materialise | Version 19.0 to 22.0 |
| Motion Capture Cameras | Qualisys | Oqus 5+ |
| Pulsed X-ray Generators | EMD Technologies | EPS 45–80 |
| Undistortion Grid | McMaster-Carr | 9255T641 |
| Wrist Implant (In-vitro Study) | Integra LifeSciences | Universal 2 |
| Wrist Implant (In-vivo Study) | Integra LifeSciences | Freedom |
| WristViz | Open-source (Brown University) | https://github.com/DavidLaidlaw/WristVisualizer/tree/master |
| X-ray Tubes | Varian Medical Systems | Model G-1086 |
| XMALab | Open-source (Brown University) | https://www.xromm.org/xmalab/ |

**Comments/Description**

Luxembourg

https://doi.org/10.1016/j.jbiomech.2019.05.040

Milwaukee, WI, USA

Rock Hill, SC, USA

CUDA-enabled GPU

Vision Research, Wayne, NJ, USA

Aurora, IL, USA

https://doi.org/10.1038/nmeth.2019

Natick, MA, USA

Leuven, Belgium

Gothenburg, Sweden

Saint-Eustache, Quebec, QC, Canada

Steel Perforated Sheet Staggered Holes, 0.048" Thk, 0.125" Hole Dia, 36" X 40"

Plainsboro, NJ, USA

Plainsboro, NJ, USA

Open-source software

Palo Alto, CA, USA

https://doi.org/10.1242/jeb.145383

**Editorial comments:**

**1. Please note that we cannot film a general protocol. We need a specific protocol with a specific sample in order to film. Can you present example data and show the processing of that data in the written protocol?**

**Response:** Yes, we can provide example data and images/videos of any sections mentioned in the written protocol.

**2. Please provide all user commands required to perform the step. This is especially important if that particular protocol step is to be filmed. We cannot film a step where all of the essential details needed to perform the step are referenced out. I have commented on the steps that need additional details in the attached manuscript.**

**Response:** We answered all your comments, and provided all necessary details.

**3. Please review the highlighting of the protocol to feature the most essential parts of your experiment. We want to film a cohesive story and this may exclude data collection and data pre-processing steps.**

**Response:** We modified the highlighted sections of the procotol. We kept data collection, pre-processing, and processing steps for the video production stages, since these are the novel and important sections of the protocol. We removed the highlighted sections of "Coordinate System Construction", "Kinematics", and "Contact Area". These steps are mostly using mathematical formulas to post-process the data.